Defocusing PTV applied to an open wet clutch: from macro to micro

Robin Leister[1] · Thomas Fuchs[2] · Jochen Kriegseis[1]

Abstract

Defocusing particle tracking velocimetry (defocusing PTV) is applied in various levels of magnification to investigate the flow in an open wet clutch with radial grooving. The magnifications range from $M = 0.8$ up to $M = 15$, whereas the corresponding defocusing sensitivities s^Z, denoting the rate of the particle image diameter change along the optical axis, range from 67.1 to 9.0 μm/pixel. For flows with sub-millimeter structures, as it is the case of this clutch flow application, a high spatial resolution is necessary to fully understand the flow phenomena in these confined geometries. It is demonstrated in this study that all optical configurations can resolve the miniature flow structures that are present in an open wet clutch. Moreover, the $M = 0.8$ set-up, featuring the largest field of view, captures the entire region between the inner and the outer radius of the clutch, providing a comprehensive overview of the three-dimensional clutch flow field, ranging from the smallest structures to the largest. It is found that the $M = 0.8$ set-up also yields the lowest uncertainties in the determination of the particle locations in x, y direction as well as in z direction along the optical axis. The particle image diameter uncertainty is $2\sigma_{d_i} = 0.24$ pixel, which translates (by multiplying the defocusing sensitivity of $s^Z = 67.1$ μm/pixel) into a particle z location determination uncertainty of $2\sigma_z = 16.1$ μm. These results give evidence to the fact that not necessarily the best defocusing sensitivity determines the accuracy of the particle z location estimation; to a great extent the signal-to-noise ratio and the width of the outer ring of the defocused particle image influence the accuracy.

Graphical Abstract
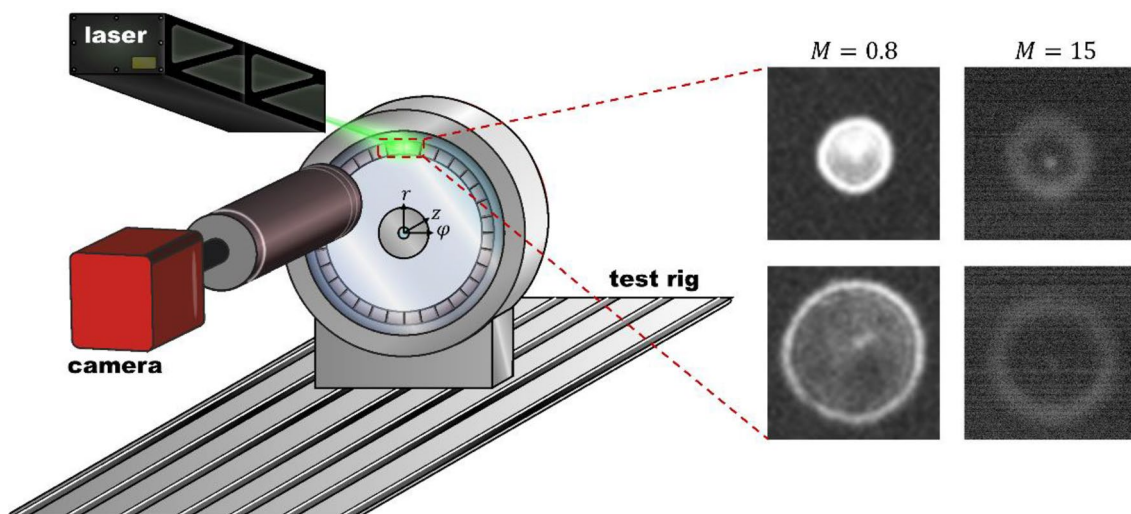
1 Introduction

The continuous development of new hybrid and battery-driven drive concepts in automotive industry, forced by the desire to save CO_2 emissions, led to a large variety of

✉ Robin Leister
   robin.leister@kit.edu

Extended author information available on the last page of the article

new energy-saving strategies. One of the strategies is the optimization of the idling behavior of wet clutches, which are installed in the majority of higher-class automobiles. The speed difference between drive and output, the sub-millimeter gap height, and the presence of oil between the disks result in a considerably high wall-shear stress, which sums up to an adverse so-called *drag torque*. The potential to reduce this quantity as energy-saving strategy was first discovered in R & D departments of industrial companies (Schade 1971; Lloyd 1974), but soon also attracted universities and research institutes with applied scientific fields (Fish 1991). A vast amount of research and development efforts addressed the minimization of this adverse torque, which mostly led to different groove patterns on one of the disk groups in the clutch package. A variety of different investigations were conducted to clarify the influence of these patterns on the basis of torque measurements (see, e.g., Neupert et al. 2018; Grötsch et al. 2019).

However, a precise experimental investigation of the cause-effect relations between disk geometry and resulting adverse drag torque has ever since been considered to be rather difficult, due to the limited availability of apt measurement techniques. When using an estimate to quantify the ongoing phenomena in the sub-millimeter gap, the use of an integral measurement method inherently leads to the loss of information and renders a precise analysis of the inter-dependency rather difficult. While the basic fluid flow without an application of grooves can be described with analytical means, as highlighted by Leister et al. (2021), this becomes more difficult with arbitrary shaped groove patterns.

This scenario is in need of an appropriate measurement technique that meets all mandatory side conditions and persists the fairly rough environment with complex geometries and accordingly high amount of reflection when investigated with laser-based velocimetry, for instance. As already shown by Leister et al. (2021a), the technique of Defocusing Particle Tracking Velocimetry (defocusing PTV) is able to extract the complete 3D3C velocity information within a radially grooved open wet clutch, as well as the resulting wall-shear-stress (WSS) on the stator.

For the present clutch flow study, different optical configurations with magnifications ranging from macroscopic ($M = 0.8$) to microscopic ($M = 15$) were used, in order to resolve different levels of detail. Thus, the $M = 0.8$ set-up with the largest field of view serves as an overview measurement, capturing the in- and outflow of the clutch gap. For the larger magnifications, it was intended to resolve the more complex small-scale flow structures in the vicinity of the groove. The significance of these flow patterns appearing in the groove domain for the overall flow field was already highlighted by Leister et al. (2021a). This study provides a comparative assessment of the different optical configurations and their performance in terms of the flow-field determination, in order to allow for the selection of the appropriate set-up for a given measurement task.

2 Defocusing PTV

2.1 Measurement principle

In general, defocusing of particle images uses the additional information of a distinct out-of-focus behavior. Historically, the technique developed out of *Particle Imaging Velocimetry* (PIV), which serves as robust and well-assessed technique for particle-based flow measurements (see e.g. Adrian and Westerweel 2011; Raffel et al. 2018). When the velocity of an individual particle is tracked, the approach is commonly referred to as *Particle Tracking Velocimetry* (PTV). Here, a variety of different techniques was developed to fit each specific need, such as 3D-PTV (Maas et al. 1993; Nishino et al. 1989), Astigmatism PTV (Cierpka et al. 2010; Kao and Verkman 1994), Shake-the-Box (Schanz et al. 2013, 2016) and Defocusing PTV. So, Defocusing PTV is one possibility among others for such a tracking and was introduced by Willert and Gharib (1992). Whenever it is necessary to resolve fine flow structures in microscopic flows, that are smaller than the light sheet thickness, it is favorable to track individual particles instead of an ensemble. An overview of most of these techniques has been published by Cierpka and Kähler (2012). After its introduction, Defocusing PTV was soon adapted to fit the micro-fluid needs, e.g., by Yoon and Kim (2006) and Pereira et al. (2007). The usage of the complete defocused image was conducted by Wu et al. (2005). Analogous, Fuchs et al. (2016) used the complete image and determined the depth by analyzing the intensity distribution at its edges.

The physical principle of defocusing can be explained visually with the help of Fig. 1. Two particles are shown, the first particle (●) is positioned on the focal plane. The second particle (●) has a certain distance to the focal plane. The first particle is imaged sharp—or in focus—with a high peak intensity as shown in the diagram of the figure. The second particle is imaged out-of-focus and consequently forms a defocused image on the camera chip. The larger the distance, the larger the image diameter and the lower the intensity. The diameter contains the explicit distance information to the focal plane. This technique is thus able to extract a three-dimensional position—in vicinity to the focal plane—with only a single camera.

The theoretical mathematical description of the particle image diameter d_i under absence of optical aberrations is
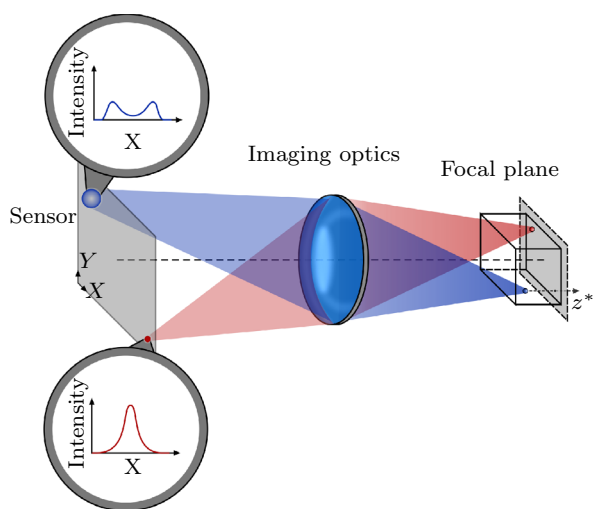
Fig. 1 Scheme of defocusing explained with two particles. The red one is located at the focal plane and imaged sharp. The blue one has a distinct distance to the focal plane and is imaged as out-of-focus particle image with a much lower peak intensity as shown in the diagrams

a sum of the geometric image, the diameter change due to diffraction and the defocusing term. This relationship has been summarized by Olsen and Adrian (2000) and can be written as

$$d_i^2 = \underbrace{M^2 \, d_p^{\,2}}_{\text{geometric image}} + \underbrace{5.95(M+1)^2 \lambda^2 f_\#^{\,2}}_{\text{diffraction}} \\ + \underbrace{\frac{M^2 z^{*2} D_a^{\,2}}{\left(s_0 + z^*\right)^2}}_{\text{defocusing}}. \tag{1}$$

Here, M appears as magnification, d_p as physical particle diameter, λ as wave length of the emitted light and $f_\#$ is the focal number of the lens. The third term models the defocusing principles and describes the diameter change of the particle on the image plane as function of the distance z^* between the particle and the focal plane, the distance s_0 between the lens and the focal plane, and the projected physical diameter of the used aperture D_a.

For practical defocusing PTV, where a linear interrelation between the particle image diameter d_i and the coordinate along the optical axis z^* is valid, this equation can be simplified further. As outlined by Olsen and Adrian (2000), $s_0 \gg z^*$ is valid for all imaging applications. With this simplification, Eq. (1) can be simplified to

$$d_i(z^*)^2 = M^2 \, d_p^{\,2} + 5.95(M+1)^2 \lambda^2 f_\#^{\,2} \\ + \frac{M^2 D_a^{\,2}}{s_0^2} z^{*2}. \tag{2}$$

This equation can be further approximated as linear interdependency when considering out-of-focus elements that have a sufficient distance to the focal plane, so that the first two terms, which are constant in regard to z^*, can be neglected. Equation (2) can thus be simplified to

$$d_i(z^*) = \frac{MD_a}{s_0} z^*. \tag{3}$$

A comparison of Eqs. (1) and (3) is visualized in Fig. 2, with the parameters given in Table 1. Given a particle image diameter for the smallest particle images of ≈ 16 px, the error between both equations can be stated as 0.36 μm,
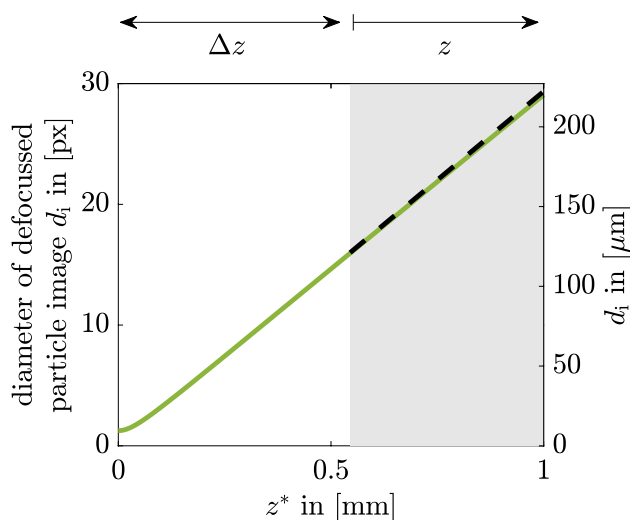

Fig. 2 Change of particle image diameter d_i according to Eqs. (1) and (3) (- -) as a function of z^*. The gray background indicates the start of the measurement region. The used parameters are summarized in Table 1

Table 1 Parameters corresponding to Fig. 2. All imaging parameters fit to the lowest magnification of $M = 0.8$ among the conducted experiments of the present study

Parameter	Symbol	Value
Magnification	M	0.8
Particle diameter	d_p	10 μm
Wave length	λ	584 nm
Focal length	f	50 mm
f-number	$f_\#$	2
Projected aperture diameter	D_a	25 mm
Lens-focal plane distance	s_0	90 mm

which corresponds to 0.047 px. To now transfer the focal plane coordinate z^* to the coordinate of the experimental set-up z, the transformation $z^* = \Delta z + z$ is applied, which is valid as visualized in Fig. 2.

The slope of Eq. (3) gives the sensitivity of the defocusing function. A link to commonly used parameters can be made by $MD_a/s_0 = s^{XY}/s^Z$ using the image reproduction scale s^{XY} in [μm/px], which is a standard imaging parameter, and the defocusing sensitivity s^Z in [μm/px], as already used by, e.g., (Fuchs et al. 2016; Leister et al. 2021a). s^Z expresses the physical change in z^*-direction if the diameter is changed by one pixel. This pixel-based values are often more meaningful, when comparing to other measurement set-ups and are used throughout the present work.

Since each commercial lens has correcting-glass elements for minimizing a vast array of aberrations (e.g., field curvature, spherical aberration, chromatic aberration), the exact intensity distribution—and thus diameter—relies on the lens and various further factors. A direct implementation of Eq. (1) would, therefore, lead to unacceptably strong deviations and errors of the position estimation.

To overcome the gap between the theoretical consideration and the desire to extract meaningful results, the present study uses the so-called *in situ* calibration approach of Fuchs et al. (2016), where the extracted diameter is locally transformed in physical units on the basis of known boundary conditions in terms of particle displacements.

2.2 Experimental set-up

An overview of the experimental set-up is given in Fig. 3 on the left, while a more detailed view of the clutch geometry is shown on the right. The stator is made from glass with a thickness of 3 mm to allow an optical access for viewing and illuminating the clutch gap. The rotor is made from aluminum, whereas exchangeable polymer clutch disks can be added depending on preference. The disks are
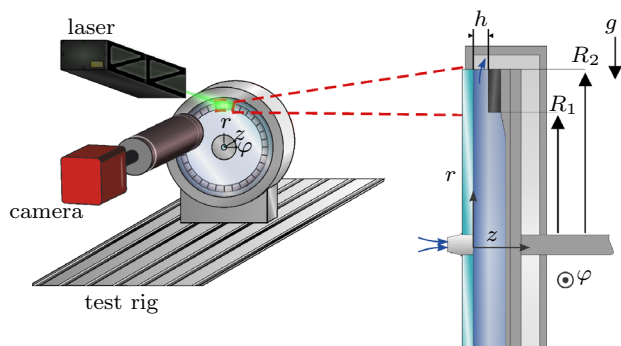

Fig. 3 Sketch of the experimental set-up (left) and the test rig (right) for the conducted defocusing PTV experiments with all relevant geometrical parameters and the used coordinate system

manufactured by 3d printing (*Formlabs Form 3 L*, layer thickness 50 μm), to allow for complex geometries and fine details of the groove patterns. The clutch geometry is characterized by the following parameters: (1) the inner radius $R_1 = 82.5$ mm; (2) the outer radius $R_2 = 93.75$ mm; (3) the gap height $h = 400$ μm between the clutch surface and the stator; (4) in case of the radially grooved clutch: the groove parameters, which are the width of $W = 1.35$ mm at the groove bottom, the groove height of $H = 1.0$ mm, and the pitch between the grooves of $11.25°$, which corresponds to 32 evenly distributed grooves along the perimeter. To suppress light reflections on the clutch surface, fluorescent melamine resin-based seeding particles with a mean diameter of $d_p = 9.84$ μm were used to seed the white mineral oil (CAS No: 8042-47-5, $\rho_0 = 850$ kg/m^3, $\nu = 16 \times 10^{-6}$ m^2/s), which is supplying the clutch. The seeding particles, emitting a wave length of $\lambda_{em} = 584$ nm, were excited at a wave length of $\lambda = 532$ nm with a double-pulsed *Quantel Evergreen* Nd:YAG laser (210 mJ). A band pass filter ($\lambda = 590 \pm 10$ nm) was placed between the camera sensor and the measurement domain, to only capture the fluorescent light of the particles.

To investigate different optical configurations, a *pco.edge 5.5* sCMOS camera was equipped with a variety of objective lens combinations, including a *Zeiss Makro-Planar f = 50 mm* lens and a *Questar QM 1* telescope, which is further referred to as a long-distance microscope. A detailed analysis of the optical characteristics of the lens combinations is outlined in the following. In particular, the use of the *Zeiss* lens, covering a macroscopic field of view, comes with optical aberrations, such as, e.g., coma, and a pronounced field curvature, both of which are reasons for the necessity to use a calibration approach that takes the local particle image characteristics into account. Along with this requirement and the fact that it is not feasible to move a calibration target in the measurement domain or to employ particles in the domain as calibration reference, the above-mentioned *in situ* calibration approach was used for evaluation, as described in detail by Fuchs et al. (2016).

2.3 Optical characteristics

Depending on the required spatial resolution, the optical set-up can be adapted in terms of varying magnifications. However, changing the optics in turn changes the imaging characteristics. Therefore, certain key parameters are assessed that characterize a defocusing PTV set-up in this section, including the magnification M, the reproduction scale s^{XY}, the FOV size, and the defocusing sensitivity s^Z. The latter parameter denotes the relation between the change of the particle-image diameter over the particle z-location, i.e., along the optical axis. In principle, this means that a stronger change of the particle-image diameter over a certain

z-distance means that the particle z-location can be determined more accurately.

Altogether four different magnifications were investigated, where the first configuration with the smallest M comprised a *Zeiss Makro-Planar f = 50 mm* at the shortest possible working distance together with a 20 mm distance ring to yield the largest possible magnification, which was still capturing the entire radial extent of the clutch gap. An overview of the parameters of all optical configurations is given in Table 2, while Fig. 4 illustrates the FOV extent in comparison with the clutch geometry. The three larger-magnified configurations comprised a *Questar QM 1* long-distance microscope as imaging optics, which was positioned at shortest possible distance of 560 mm. Here, the magnification was adjusted by adding magnifying lenses between the camera and the lens. Note that the FOV size for the *Zeiss 50 mm* configuration was cropped due to optical distortions in the image corners, whereas for the *Questar* configurations the entire sensor was used.

In terms of the accuracy of the particle z-location determination, the defocusing sensitivity s^Z, as listed in the last column of Table 2, is a decisive factor. With increasing magnification s^Z decreases, which means that with a certain change of the particle z-location, the particle-image diameter increases/decreases by a larger amount. However, it becomes apparent that s^Z does not scale linearly with M, since for the first two set-ups (*Zeiss* 50 mm and *Questar* + 2×), the M ratio yields around 6, while s^Z ratio yields around 3 (cp. first two rows in Table 2). This is due to the fact that with different lens configurations quantities such as the aperture diameter, D_a, change. As can be seen from Eq. (1), D_a changes the slope of the relation between z and the particle-image diameter. Considering only at the *Questar* configurations, also *Questar* + 6× does not scale linearly with the magnification. The reason for this is the addition of magnifying lenses, which actually changes the largest opening diameter of the light path D_a.
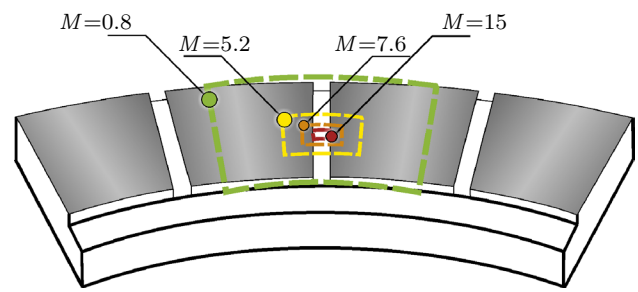

Fig. 4 Overview of the FOV locations and the corresponding magnifications, M, for all optical configurations listed in the first column of Table 2

Figure 5 shows a double frame image for the lowest magnification of $M = 0.8$. The recordings were evaluated as outlined in Fuchs et al. (2016), providing a detailed description of the *in situ* calibration procedure as well as the particle image diameter, d_i, determination scheme. In this approach, d_i is defined as the location where the intensity of the outer ring of the defocused particle image at the 4 vertices—i.e., the extrema of the extent of the particle image in sensor X and Y direction—first reaches a normalized, particle image-specific intensity threshold, approaching the image center from beyond the outer ring of the defocused particle image. After evaluating the particle image diameters in the recordings, a relation between the particle image sensor location (X, Y), the particle image diameter d_i and the physical particle $(x, y,$ and $z)$ needs to be established.

Table 2 Optical parameters for the different optical configurations, where s^{XY} denotes the reproduction scale and s^Z the defocusing sensitivity in [μm/pixel]

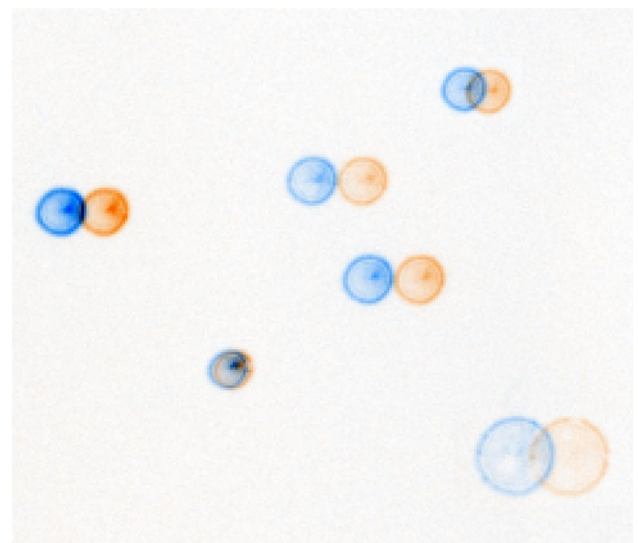| Configuration	M	FOV	s^{XY}	s^Z
	[-]	[mm²]	[μm/px]	[μm/px]
• *Zeiss* 50 mm	0.8	12 × 12	7.57	67.1
• *Questar* + 2×	5.2	3.2 × 2.7	1.25	23.4
• *Questar* + 3×	7.6	2.2 × 1.8	0.86	15.5
• *Questar* + 6×	15	1.1 × 0.9	0.43	9.0

Fig. 5 False colored, gray scale, cropped, double frame raw image for configuration • $M = 0.8$; Frame A (•), Frame B (•). The intensity was inverted for visual purposes. The image was acquired with a *Zeiss 50 mm f2 macro* lens

To do so, the particle image displacement field is determined from the set of double-frame recordings, resulting in a distribution of displacements (ΔX, ΔY, and Δd_i) and the corresponding coordinates (X, Y, and Δd_i). Further consideration of the no-slip condition provides two boundary conditions for the present case of a clutch flow: (1) the displacements approach zero at the clutch stator plate, whereas (2) the displacements match the circumferential velocity at the clutch rotor. Taking these boundary conditions into account, the application of a linear fit to the particle image displacements close to the rotor or the stator yields a d_i value, which represents a particle at the stator or rotor wall. In the present configuration, the particle image diameter increases from the stator toward the rotor, which means that the focal plane is located closer to the camera than the measurement domain. With the knowledge of the gap height between the clutch rotor and stator, or the clutch rotor groove depth, these particle image diameters can then be transferred into a physical location, since the particle image diameter changes linearly along the optical axis, as it was demonstrated in Sect. 2.1. Some further details on the evaluation method, specifically for this clutch flow application, can also be found in the treatise of Leister et al. (2021a). The subsequent section addresses the accuracy of the particle z-location in relation to the defocusing sensitivity s^Z.

3 Results

3.1 Particle location uncertainty

As already generally outlined from a theoretical perspective in Sect. 2.1, a stronger rate of change of the particle-image diameter over the particle z-location, i.e., along the optical axis, yields an increased resolution. Theoretically, at a given numerical aperture, higher magnifications, leading to lower s^Z-values, should have a higher particle location accuracy. However, changing the optical configuration also changes the imaging characteristics and, therefore, the appearance of the particle images. Thus, the intensity distribution of the particle images change, which in turn also changes the signal-to-noise ratio (SNR), among other factors. For the optical configurations presented in this study, the relation between s^Z and the uncertainty of the particle z-location determination are estimated in the following to elaborate on the applicability of the theoretical considerations for the problem at hand.

In an attempt to estimate the particle location determination uncertainty from the measurement data, it is assumed that velocity component u_z approaches zero in the vicinity of the stator. It has been demonstrated in previous studies by Leister et al. (2021a) and Leister et al. (2022) that this assumption holds true for the purpose of this uncertainty estimation procedure. With u_z being close to zero, the change of the particle image diameter between a double-frame recording is supposed to be close to zero as well. However, as a consequence of the uncertainty in the particle image diameter determination procedure, the particle image diameter varies. Using the defocusing sensitivity, s^Z, the standard deviation of this particle image diameter variation, σ_{d_i}, can be translated into the particle z location determination uncertainty, σ_z, by multiplication, i.e.,

$$\sigma_z = \sigma_{d_i} \cdot s^Z. \tag{4}$$

Table 3 gives an overview of the uncertainty values for each optical configuration, revealing that $2\sigma_{d_i}$ is the lowest with a value of 0.24 pixels, for the *Zeiss* lens. The diameter uncertainty is one order of magnitude larger for the *Questar* configurations, reaching up to almost 11 pixels. Intuitively, it might seem obvious that the set-ups with the significantly larger magnifications of up to $M = 15$ (which is 19 times larger than the *Zeiss* lens configuration) yield better spatial resolutions. However, the values in Table 3 clearly prove the first-glance intuition wrong. In fact, the set-up with the largest magnification shows the highest uncertainty in the particle image location determination, being 6 times larger than for the *Zeiss* lens. The other *Questar* configurations show an uncertainty increased by a factor of 3. Relative to the measurement depth of around 1400 μm, the uncertainty of the particle z location determination yields only 1.17% for the *Zeiss* lens.

The lower performance of the *Questar QM 1* optics has a variety of reasons. One is that the minimum working distance of around 560 mm is relatively large: compared to a microscope objective with a small working distance of less than 10 mm used by Fuchs and Kähler (2019), at a similar magnification (13 vs. 15, here), the defocusing sensitivity was $s^Z = 2.05$ μm/pixel, whereas here a value of only 9.0 was achieved. Moreover, the optical characteristics of the *Questar* lead to particle image shapes where the defocused ring is spread out over around 20 pixels combined with a

Table 3 For the different optical configurations: the uncertainty of the particle-image diameter determination, $2\sigma_{d_i}$, and the related uncertainty of the particle z-location determination, $2\sigma_z$

Configuration	M [-]	$2\sigma_{d_i}$ [pixel]	$2\sigma_z$ [μm]
• *Zeiss* 50 mm	0.8	0.24	16.4
• *Questar* + 2×	5.2	2.12	49.6
• *Questar* + 3×	7.6	3.12	48.4
• *Questar* + 6×	15	10.98	98.8

(a) • $M = 0.8$;
(b) • $M = 5.2$;
(c) • $M = 7.6$;
(d) • $M = 15$;
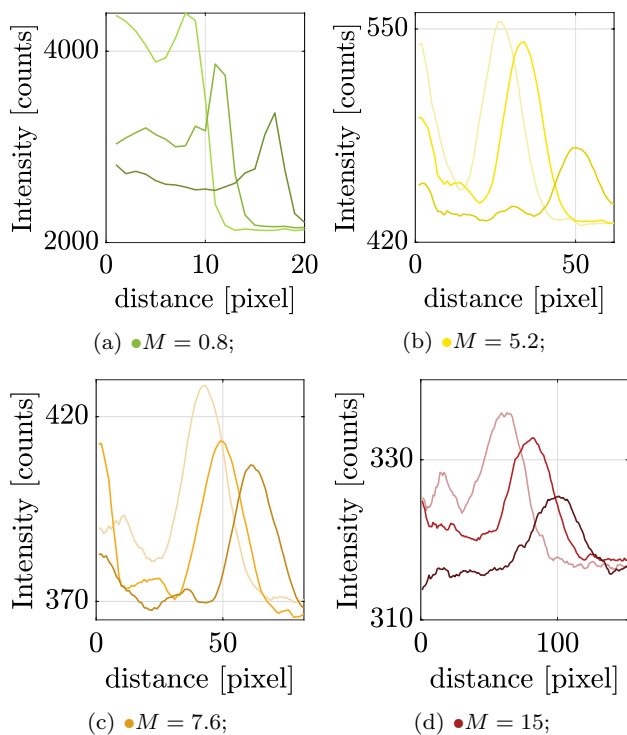
Fig. 6 Radial intensity distribution of three exemplary particle images for each magnification

Fig. 7 Comparison of the circumferential velocity u_φ and the standard deviation σ_{u_φ} at $\varphi R_\mathrm{m}/W = 0.5$ along z for all magnifications (• $M = 0.8$; • $M = 5.2$; • $M = 7.6$; • $M = 15$)

very noisy intensity distribution that barely exceeds the background intensity (see Fig. 6 for the examples of the intensity distribution). In terms of the SNR, this result is a significant detriment relative to the *Zeiss* lens, since for the latter, the defocused ring has a width of around 3 pixels with a very distinct intensity distribution. These conditions are perfect for determining the edge location of the particle images with high accuracy. Comparing the σ_{d_i} values achieved in this experiment using the *Zeiss* lens against earlier findings by Fuchs et al. (2016), it becomes apparent that the uncertainty here is significantly lower, ~ 0.25 pixel vs. ~ 1 pixel before, even though the optical configuration was similar. However, in the current experiment seeding particles with a diameter of 10 μm were used in a liquid flow, whereas in the previous study an air flow using DEHS particles with a diameter of around 0.35 μm was used. As a result the SNR was lower and so is the accuracy of the diameter estimation, which is also observed when comparing the *Questar* configurations with the *Zeiss* configuration in the present study.

3.2 Fluid mechanic outcomes

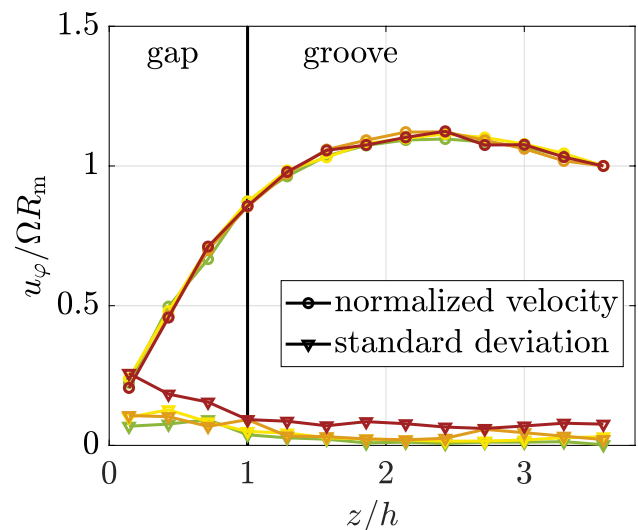The previous sections focused on the accuracy of each magnification, while the present section takes the fluid mechanic results into consideration. The smallest magnification of $M = 0.8$ enables an investigation along the entire radius of interest. This is important knowledge in terms of an applicability for clutch manufacturers, since such information up-to-now has only been achieved with numerical efforts. A considerably wide FOV, with an accuracy, that is sufficient to depict the most important fluid mechanic phenomena, is beneficial for this flow scenario.

As benchmark comparison case, the middle of the groove at $\varphi R_\mathrm{m}/W = 0.5$ and $r = R_\mathrm{m} \pm 500$ μm is chosen, since all magnifications recorded this area. Figure 7 shows the normalized circumferential velocity u_φ along the normalized z-coordinate in the middle of the groove at $\varphi R_\mathrm{m}/W = 0.5$ for all FOVs. To enable a fair comparison between all setups, the same amount of particles were used (≈ 500). The z-values were divided in 100 μm divisions. All velocity data are normalized with their corresponding disk velocity ΩR_m, since small deviations of the velocity existed over the different experiments.

Additionally, the standard deviation σ_{u_φ} is shown for each magnification and z-bin. As already indicated earlier in Sect. 3.1, the trend of a lower uncertainty for the smallest magnification is not only visible for the spatial consideration, but also within the velocity data. The highest magnification yields the largest velocity uncertainty. The reason is similar to the already discussed spatial accuracy. The standard deviation in the gap region is mainly introduced to the higher velocity gradient and a finite fragmentation of the z-binning. For the largest magnification, additionally some outliers at low z-coordinates make a noticeable influence.

Note that the error is relatively constant within the groove. Only for the highest magnification, a slight increase at the largest z/h-values is visible, which indicates a too low SNR at this part for this specific parameter combination.

4 Conclusions

In this study, the flow in an open wet clutch was investigated using optical magnifications ranging from $M = 0.8$ up to $M = 15$, with the intent to increase the resolution of the flow field with increasing magnification. It has been found that all optical configurations were capable of capturing the flow field, including the sub-millimeter flow structures in the clutch rotor grooves. For the $M = 15$ set-up, even the particle images with very low signal-to-noise ratios of only 10 counts above the background intensity were successfully detected and evaluated.

Counter-intuitively, the optical configuration with the lowest magnification—a *Zeiss* macro-objective lens—yielded the smallest particle location determination uncertainty, and as such the best spatial resolution. The set-ups ($M = 5 - 15$) using the *Questar QM1* long-distance microscope were outperformed in terms of the particle z location determination uncertainty by a factor of 3, at least. Hence, the signal-to-noise ratio of the particle images as well as the thickness of the outer ring of the defocused particle image have more impact on the particle location determination uncertainty than the fact that the particle image diameter increases at a higher rate with z for the *Questar QM1* configurations.

It has to be emphasized that these results apply for imaging set-ups with working distances larger than 100 mm, where microscopic imaging optics are referred to as long-distance microscopes. With standard microscope objectives, significantly better particle location determination accuracies than the optics investigated in this study can be achieved. However, simply using standard microscope objectives (which promise the highest accuracy in particle location determination) instead of the long-distance microscope lenses is not feasible for several reasons:

First, the geometric and assembly constraints do not allow for placing imaging lenses close to the clutch. Second, the measurement depth of more than 1 mm would yield particle image sizes of several hundred pixels due to the large defocusing sensitivity. As a result the seeding concentration would have to be low and the low SNR of these very large particle images would make the particle location determination inaccurate with distance to the focal plane. Altogether, it showed that the *Zeiss* lens with the relatively low magnification of only $M = 0.8$ was both able to resolve the small-scale flow features, while at the same time being able to capture a large field of view. As such, this configuration allowed for a comprehensive investigation of the entire clutch flow domain without the necessity of measuring at different locations. Consequently, the latter optical configuration can be considered suitable for performing extensive parameter studies over a variety of clutch geometries and operating conditions, as is as yet pending in rigorous industry-like clutch-design optimization efforts.

Finally, the quantification of the particle image signal-to-noise ratio influence on the particle-location determination remains an open question, leaving room for a future experimental assessment.

Declarations

Conflict of interest The authors declare no competing interest.

Ethical approval Not applicable.

References

Adrian RJ, Westerweel J (2011) Particle image velocimetry. Cambridge University Press, Cambridge

Cierpka C, Kähler CJ (2012) Particle imaging techniques for volumetric three-component (3d3c) velocity measurements in microfluidics. J Visual 15(1):1–31. https://doi.org/10.1007/s12650-011-0107-9

Cierpka C, Segura R, Hain R, Kähler CJ (2010) A simple single camera 3c3d velocity measurement technique without errors due to depth of correlation and spatial averaging for microfluidics. Meas Sci Technol 21(4):045401. https://doi.org/10.1088/0957-0233/21/4/045401

Fish RL (1991) Using the sae #2 machine to evaluate wet clutch drag losses. SAE Trans 100:1041–1054

Fuchs T, Hain R, Kähler CJ (2016) In situ calibrated defocusing Ptv for wall-bounded measurement volumes. Meas Sci Technol 27(8):084005. https://doi.org/10.1088/0957-0233/27/8/084005

Fuchs T, Kähler CJ (2019) Single axis volumetric μ PTV for wall shear stress estimation. In: Kähler CJ, Hain R, Scharnowski S, Fuchs T (eds) Proceedings of the 13th international symposium on particle image velocimetry, https://athene-forschung.unibw.de/doc/129386/129386.pdf

Grötsch D, Niedenthal R, Völkel K, Pflaum H, Stahl K (2019) Effiziente CFD-Simulationen zur Berechnung des Schleppmoments nasslaufender Lamellenkupplungen im Abgleich mit Prüfstandmessungen. Forsch Ingenieurwes 83:227–237. https://doi.org/10.1007/s10010-019-00302-3

Kao H, Verkman A (1994) Tracking of single fluorescent particles in three dimensions: use of cylindrical optics to encode particle position. Biophys J 67(3):1291–1300. https://doi.org/10.1016/s0006-3495(94)80601-0

Leister R, Najafi AF, Kriegseis J, Frohnapfel B, Gatti D (2021) Analytical modeling and dimensionless characteristics of open wet clutches in consideration of gravity. Forsch Ingenieurwes 85(4):849–857. https://doi.org/10.1007/s10010-021-00545-z

Leister R, Fuchs T, Mattern P, Kriegseis J (2021) Flow-structure identification in a radially grooved open wet clutch by means of defocusing particle tracking velocimetry. Exp Fluids. https://doi.org/10.1007/s00348-020-03116-0

Leister R, Pasch S, Kriegseis J (2022) On the applicability of LDV profile-sensors for periodic open wet clutch flow scenarios. Exp Fluids. https://doi.org/10.1007/s00348-022-03487-6

Lloyd FA (1974) Parameters contributing to power loss in disengaged wet clutches. SAE Trans 83:2498–2507

Maas HG, Gruen A, Papantoniou D (1993) Particle tracking velocimetry in three-dimensional flows. Exp Fluids 15(2):133–146. https://doi.org/10.1007/bf00190953

Neupert T, Benke E, Bartel D (2018) Parameter study on the influence of a radial groove design on the drag torque of wet clutch discs in comparison with analytical models. Tribol Int 119:809–821. https://doi.org/10.1016/j.triboint.2017.12.005

Nishino N, Kasagi N, Hirata M (1989) Three-dimensional particle tracking velocimetry based on automated digital image processing. J Fluids Eng 111(4):384–391. https://doi.org/10.1115/1.3243657

Olsen MG, Adrian RJ (2000) Out-of-focus effects on particle image visibility and correlation in microscopic particle image velocimetry. Exp Fluids 29(7):S166–S174. https://doi.org/10.1007/s003480070018

Pereira F, Lu J, Castaño-Graff E, Gharib M (2007) Microscale 3d flow mapping with μDDPIV. Exp Fluids 42(4):589–599. https://doi.org/10.1007/s00348-007-0267-5

Raffel M, Willert CE, Scarano F, Kähler CJ, Wereley S, Kompenhans J (2018) Particle image velocimetry. Springer, Berlin

Schade CW (1971) Effects of transmission fluid on clutch performance in farm construction and industrial machinery meeting. SAE Int. https://doi.org/10.4271/710734

Schanz D, Gesemann S, Schröder A (2016) Shake-the-box: Lagrangian particle tracking at high particle image densities. Exp Fluids. https://doi.org/10.1007/s00348-016-2157-1

Schanz D, Schröder A, Gesemann S, Michaelis D, Wieneke B (2013) 'Shake The Box': A highly efficient and accurate Tomographic Particle Tracking Velocimetry (TOMO-PTV) method using prediction of particle positions. In: PIV13; 10th international symposium on particle image velocimetry – ISPIV, conference proceedings, TU Delft, Delft, http://resolver.tudelft.nl/uuid:212b0c2d-3210-482f-b751-91d98d5ea43d

Willert CE, Gharib M (1992) Three-dimensional particle imaging with a single camera. Exp Fluids 12(6):353–358. https://doi.org/10.1007/BF00193880

Wu M, Roberts JW, Buckley M (2005) Three-dimensional fluorescent particle tracking at micron-scale using a single camera. Exp Fluids 38(4):461–465. https://doi.org/10.1007/s00348-004-0925-9

Yoon SY, Kim KC (2006) 3d particle position and 3d velocity field measurement in a microvolume via the defocusing concept. Meas Sci Technol 17(11):2897–2905. https://doi.org/10.1088/0957-0233/17/11/006

Authors and Affiliations

Robin Leister[1] · **Thomas Fuchs[2]** · **Jochen Kriegseis[1]**

1   Institute of Fluid Mechanics (ISTM), Karlsruhe Institute of Technology (KIT), Kaiserstr. 10, 76131 Karlsruhe, Germany

2   Institute of Fluid Mechanics and Aerodynamics, Universität der Bundeswehr München, Werner-Heisenberg-Weg 39, 85577 Neubiberg, Germany